This is a repository copy of *Concurrent La and A-Site Vacancy Doping Modulates the Thermoelectric Response of SrTiO3: Experimental and Computational Evidence.*.

White Rose Research Online URL for this paper:
http://eprints.whiterose.ac.uk/125290/

Version: Accepted Version

Concurrent La and A-site Vacancy Doping Modulates the Thermoelectric Response of SrTiO$_3$. Experimental and Computational Evidence

Feridoon Azough[1], Samuel S. Jackson[1], Dursun Ekren[1], Robert Freer[1*]

Marco Molinari[2,3], Stephen R. Yeandel[2,4], Pooja M. Panchmatia[4], Stephen C. Parker[2*]

David Hernandez Maldonado[5], Demie M. Kepaptsoglou[5], Quentin M. Ramasse[5]

[1]School of Materials, University of Manchester, Manchester M13 9PL, UK

[2]Department of Chemistry, University of Bath, Claverton Down, Bath, BA2 7AY, UK

[3]Department of Chemistry, University of Huddersfield, Queensgate, Huddersfield, HD1 3DH, UK

[4]Department of Chemistry, Loughborough University, Epinal Way, Loughborough, LE11 3TU, UK

[5]SuperSTEM Laboratory, SciTech Daresbury Campus, Keckwick Lane, Warrington, WA4 4AD, UK

ABSTRACT: To help understand the factors controlling the performance of one of the most promising n-type oxide thermoelectrics SrTiO$_3$, we need to explore structural control at the atom level. In Sr$_{1-x}$La$_{2x/3}$TiO$_3$ ceramics ($0.0 \leq x \leq 0.9$), we determined that the thermal conductivity can be reduced and controlled through an interplay of La substitution and A-site vacancies and the formation of a layered structure. The decrease in thermal conductivity with La and A-site vacancy substitution dominates the trend in the overall thermoelectric response. The maximum dimensionless Figure of merit is 0.27 at 1070 K for composition $x = 0.50$ where half of the A-sites are occupied with La and vacancies. Atomic resolution Z-contrast imaging and atomic scale chemical analysis show that as La content increases, A-site vacancies initially distribute randomly ($x < 0.3$), then cluster ($x \sim 0.5$), and finally form layers ($x = 0.9$). The layering is accompanied by a structural phase transformation from cubic to orthorhombic, and the formation of 90° rotational twins and anti-phase boundaries leading to the formation of localized supercells. The distribution of La and vacancies contributes to a non-uniform distribution of atomic scale features. This combination induces temperature stable behaviour in the material and reduces thermal conductivity, an important route to enhancement of the thermoelectric performance. A computational study confirmed that the thermal conductivity of SrTiO$_3$ is lowered by the introduction of La and vacancies as shown by the experiments. The modelling also predicts that the thermal conductivity at high La content can be further reduced when A-site vacancies are randomly distributed, rather than forming layers.

INTRODUCTION

Thermoelectric (TE) energy conversion is widely recognized as a promising technology for both electric power generation through waste heat recovery and cooling of electronic devices.[1] To achieve impact, TE technology must be affordable and effective; this depends critically on the TE performance of the materials. Metal oxide materials are attractive candidates[2-4] compared to conventional TE materials because of their affordable large scale production, elemental abundance, low toxicity, and stability in oxidising conditions and at high temperatures.[5] The effectiveness of a material to convert waste heat into electricity is given by the dimensionless figure of merit (ZT), which is maximized by increasing electrical conductivity and

reducing thermal conductivity.[2] In general it is argued that the material must have a peak ZT greater than 1, or at least more than 0.5 over a wide temperature range to be commercially valuable.

Whereas p-type oxide materials (e.g. Na_xCoO_2, $Ca_3Co_4O_9$, $Bi_2Sr_2Co_2O_y$)[6-9] were the first to show competitive thermoelectric properties, the development of an outstanding n-type material has proved more challenging. Most of the proposed n-type materials, including $CaMnO_3$,[10-12] $SrTiO_3$,[2, 13-20] and $Ba_{6-3x}Nd_{8+2x}Ti_{18}O_{54}$,[21,22] are based on the perovskite and tungsten bronze structures. Of these the perovskite structured materials have been at the center of recent development of n-type high temperature thermoelectric ceramics, particularly materials based on $SrTiO_3$. Both experimental and computational methodologies aid the design and engineering of desirable thermoelectric structures with enhanced material properties. Successful applications have been related to both nanostructuring[2,20] and band engineering.[3,11,21] However, the major advantage of the ABO_3 perovskite structure is its ability to accommodate dopants on both the B-site and on the A-site. One of the most promising substitutions is with a trivalent cation, A^{3+}, into $A^{2+}BO_3$, which can be accommodated by the introduction of vacancies in the A sub-lattice, such as in the solid solution $SrTiO_3$-$La_{2/3}TiO_3$ (i.e. $Sr_{1-x}La_{2x/3}TiO_3$).[15, 16, 23] This has led to very encouraging TE properties, which are sensitive to the structures of the materials.[2, 16]

At room temperature, $SrTiO_3$ has a perovskite, aristotype, cubic structure, with lattice parameter of a=3.905Å and space group $Pm\bar{3}m$.[24] The structure remains cubic up to the melting point. The $La_{2/3}TiO_3$ end member can be stabilized by small additions, less than 10%, of a perovskite compound such as $LaAlO_3$, $CaTiO_3$ or $SrTiO_3$.[25-27] The structure of this end member is characterized by layered ordering of La cations onto the perovskite A-sites, such that one layer of the A-sites is essentially fully occupied by La cations and the next layer is shared between La and A-site vacancies.[28, 29] This cation-vacancy ordering reduces the symmetry to tetragonal, and leads to the doubling of the c-parameter (relative to that in the parent perovskite). The space group is $P4/mmm$. The tetragonal symmetry is stable to about 400ºC. The room temperature structure shows an orthorhombic distortion with lattice parameters doubled in all three directions with $Cmmm$ as space group.[29] Using X-ray diffraction and high-resolution transmission electron microscopy (HRTEM) Battle et al. directly observed Sr/La sub-lattice features in perovskite structure $Sr_{1-3y/2}La_yTiO_3$ ($0.25 \leq y \leq 0.6$).[30]

This A site doping strategy with $SrTiO_3$ has the advantage of lowering the high thermal conductivity (approximately $11.0 - 3.2$ W/m.K in the temperature range of 300 ~ 1000 K)[15] via a structural change of the parent material, which depending on the La^{3+} content may form a layered structure. Reduction of lattice thermal conductivity is essential to improve the thermoelectric response of $SrTiO_3$ based materials.

We have already demonstrated that there is an ordered distribution of A-site vacancies in $La_{2/3}TiO_3$ stabilized with $LaAlO_3$ perovskite.[31] In the present study, we employed experimental and computational techniques, including atomic level imaging and chemical characterization using scanning transmission electron microscopy (STEM) high-angle annular dark field (HAADF) and electron energy loss spectroscopy (EELS), along with molecular dynamics calculations to explain the role of the doping (A-site vacancy – cation distribution), the layering formation with increased La content, and the role of sub-grain features associated with the crystal structure in the $SrTiO_3$-$La_{2/3}TiO_3$ system. This provides a route to determine the complex structure – thermal conductivity property relationships and a means to improve the material's thermoelectric properties through design and engineering. The prime objective of this study is thus to understand thermal transport in perovskite structured oxides, and specifically factors other than oxygen vacancies. For this reason the focus is the behavior of samples prepared under oxidizing conditions so that the additional complexities of oxygen vacancies are eliminated. Thermal and electrical data are presented for samples prepared under both oxidizing and reducing conditions to set the results in context.

METHODS

Experimental Methodology. Polycrystalline samples of $Sr_{1-x}La_{2x/3}TiO_3$ (x = 0.0, 0.1, 0.3, 0.5, 0.7 and 0.9, hereafter denoted as x0, x10 etc.) were produced by standard solid-state reaction techniques. All powders were 99.9% purity and obtained from Sigma Aldrich. The La_2O_3 was first dried at 1173 K for 6 h prior to mixing with TiO_2 and $SrCO_3$ in the required stoichiometric ratios. The powders were mixed in a vibratory mill for 18 hours with 8 mm Zr balls and propan-2-ol in a 1:1:1 ratio. After drying the powders were calcined for 4 h at 1373 K, then re-milled under the conditions described above and dried before pressing in a 20 mm die in a uniaxial press at 25 MPa.

The compacts were sintered at 1733 K for 4 h in air, and then cooled at the slow rate of 60˚C/h to avoid oxygen loss. One set of samples was sintered under reducing atmosphere (Ar-5% H_2) at 1733 K for 4 hours. The thermoelectric response of all samples was evaluated. Samples labelled with the

letter "A" were air sintered, whilst those labelled "H" were sintered under reducing conditions.

Samples for X-ray diffraction were cut and then ground using 4000 SiC paper. X-ray diffraction was performed with a Philips X'Pert Pro diffractometer with 0.0084^0 step size (4 s per step) between 5^0 and 80^0. Rietveld analysis of the data was undertaken using TOPAS 4.2 software (Bruker AXS, Karlsruhe, Germany).[32]

The microstructure of the polished surface of the samples was analysed using a Philips® XL30 field emission gun (FEG)-SEM HKL® equipped with an energy-dispersive X-ray (EDX) detector.

Samples for TEM and STEM investigation were prepared by both standard crushing and ion beam thinning techniques. For ion beam-thinning, specimens were first ground on 1200 grade SiC to reduce the thickness to ~300 μm. They were ultrasonically cut into 3 mm diameter disks (Model KT150; Kerry Ultrasonic Ltd.) then dimpled (Model D500; VCR Group, San Francisco, CA) to reduce the thickness of the centre of the disk to 30 μm. Finally, the disks were ion beam thinned (using a Gatan precision ion polishing system model 691; PIPS[TM]) operating at 4–6 kV. For the crushing method, the sintered disks were crushed to powder using an agate mortar and pestle. Grains of individual powders were dispersed in chloroform, dropped onto a copper grid covered with a holey carbon film, and then dried. Structures were initially investigated using selected area electron diffraction (SAED) and high-resolution transmission electron microscopy (HRTEM) techniques using a FEI FEGTEM (Tecnai G2, Hillsboro, OR) operating at 300 kV. Subsequently, atomic level resolution level structural characterization was carried out using an aberration-corrected Nion microscope (UltraSTEM100; Nion Company, Kirkland, WA) located at the Daresbury SuperSTEM Laboratory in the United Kingdom.

Thermal conductivity was obtained from measurement of the density (Archimedes method), thermal diffusivity (laser flash, built in-house) and heat capacity (Netzsch STA 449 C) both in an Ar atmosphere. For thermal diffusivity measurements the pellets were 10 mm in diameter, 1 mm thick, polished to a 1 μm finish and coated in graphite. For heat capacity measurements the pellets were 4 mm in diameter and the surface polished to a 1 μm finish.

An ULVAC® ZEM-3® was used to determine the electrical conductivity and Seebeck coefficients of all the samples from temperature to 1100 K.

Computational Methodology. The thermal conductivity was calculated using the Green-Kubo method[33,34] as implemented in the classical molecular dynamics code LAMMPS[35] (Large-scale Atomic/Molecular Massively Parallel Simulator). All calculations were performed using the partial-charge rigid-ion potential model developed by Teter[36] as detailed in Table 1. All structures were simulated in the temperature range of 500-1100 K. At each temperature, each structure was equilibrated for 50 ps with a time step of 1 fs using an NPT triclinic ensemble with a Nose–Hoover thermostat and barostat. The lattice vectors were averaged every 10 fs and the averaged vectors were then imposed on the final structure for the heat-flux data collection. Heat-flux data was collected for 20 ns sampling every 10 fs. The heat-flux was numerically autocorrelated and integrated to give thermal conductivity as a function of decay time, which was then averaged over a portion of the integral to reduce the noise in the thermal conductivity.[37]

All structural models were designed using the METADISE code.[38] Three materials were selected for in-depth modeling, corresponding to experimental compositions of x20, x50, and x90. Composition x20 has low A-site vacancy and lanthanum concentrations, x50 is the mid-point in the range, and x90 has high A-site vacancy and lanthanum concentrations. The models were generated to reflect the structural features of experimental samples inferred from X-ray and STEM-HAADF-EELS data, which include a layered structure as the La and A-site vacancy concentrations increase. As well as having three different compositions, each composition was modelled for three different structural configurations, which enabled us to compare and ultimately predict designs for functional materials with enhanced properties. Configuration xNRand (N = 20, 50, 90) has La, Sr, and vacancies randomly distributed across all A-sites, which produces configurations with no layering of any A-site species. Configuration xNLaSr (N = 20, 50, 90) has alternating layers, one with A sites fully occupied by La and the other partially occupied by Sr, La and vacancies. Configuration xNLaV (N = 20, 50, 90) has alternating layers, one with A sites occupied by La and vacancies and the other (A-site) layer fully occupied by Sr or La.

Table 1. The potential model developed by Teter[36] with the interactions based on Buckingham potential forms between cations and anions. Partial charges are superscripted.

Interaction	A (eV)	ρ (Å)	C (eV×Å⁶)
$O^{-1.2}$-$O^{-1.2}$	1844.75	0.3436	192.58
$Sr^{-1.2}$-$O^{-1.2}$	14566.64	0.2450	81.77
$La^{1.8}$-$O^{-1.2}$	4369.39	0.2786	60.28

|			
Ti$^{2.4}$-O$^{-1.2}$	23707.91	0.1856	14.51

RESULTS AND DISCUSSION

Structural Bulk Properties. High density (> 97% theoretical) crack-free sintered samples were produced for all air sintered $Sr_{1-x}La_{2x/3}TiO_3$ formulations. Samples sintered under reducing conditions were of marginally lower density, but generally 95% dense and above. The density data (i.e. experimental values and % theoretical values) for the samples are shown in Table 2. Half the ceramics were sintered in air to reduce the effect of oxygen vacancies and electronic contribution (Ti^{3+}) on the thermal properties of the material. This enables us to focus on the contribution due to La and A-site vacancy doping. The remaining samples were sintered under reducing conditions for comparison purposes.

Phase Analysis. XRD spectra for the $Sr_{1-x}La_{2x/3}TiO_3$ materials sintered in air are presented in Figure 1. All the spectra could be refined based on a perovskite structure without the presence of reflections arising from impurity phases. The XRD results indicate that the $La_{2/3}TiO_3$ end member, i.e. sample x90, can be stabilized by $SrTiO_3$. This was already proven for $LaAlO_3$[39] and $CaTiO_3$.[26] Rietveld refinement for samples x10 and x90 showed a cubic ($Pm\overline{3}m$) structure and an orthorhombic ($Cmmm$) structure respectively. Sample x30 contains a tetragonal, $I4/mcm$ phase in addition to a cubic phase and samples x50 and x70 contain an $I4/mcm$ phase in addition to an orthorhombic $Cmmm$ phase. The phase content of the $Sr_{1-x}La_{2x/3}TiO_3$ ceramics sintered in air is presented in Table 2. Data for samples sintered under reducing conditions are not significantly different. The results in Figure 1 and Table 2 support the work of Howard et al. [27, 28] and Lu et al [40] for the $Sr_{1-x}La_{2x/3}TiO_3$ system, and agree with the findings of Kovalevsky et al [41] for the structural changes at the $SrTiO_3$ rich end of the $SrTiO_3$-$Pr_{2/3}TiO_3$ system. The refined lattice parameters are summarized in Figure 2.

Table 2. Density and phase content data for the $Sr_{1-x}La_{2x/3}TiO_3$ ceramics.

$Sr_{1-x}La_{2x/3}TiO_3$	Expt. Density (g cm^{-3})	Theoretical Density (%)	Cubic Phase (%)	Tetragonal Phase (%)	Orthorhombic Phase (%)
X0A	5.08 ± 0.092	99.2	100	-	-
X10A	5.100 ± 0.096	99.1	100	-	-
X10H	5.094 ± 0.087	98.9			
X30A	5.093 ± 0.048	98.1	12	88	-
X30H	4.915 ± 0.018	95.3			
X50A	5.126 ± 0.024	97.9	-	77	23
X50H	5.124 ± 0.024	97.3			
X70A	5.132 ± 0.095	97.2	-	7	93
X70H	5.023 ± 0.016	94.9			
X90A	5.252 ± 0.046	98.4	-	-	100
X90H	4.972 ± 0.019	92.0			
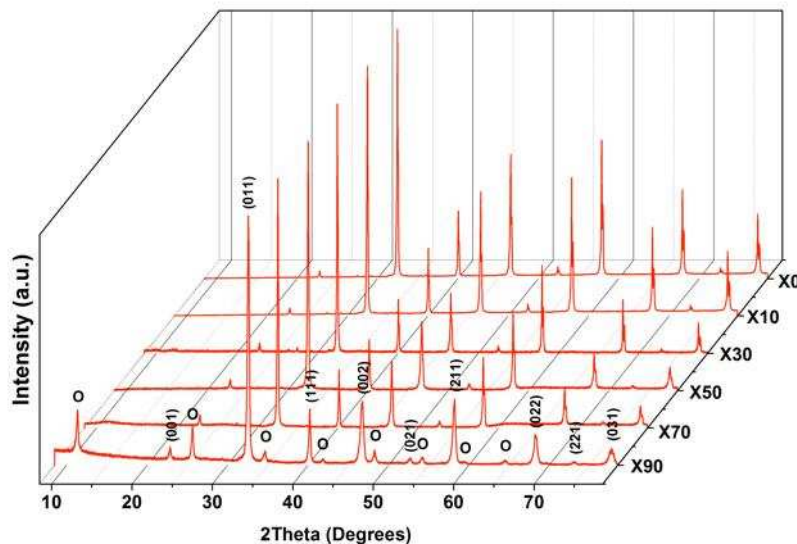
Figure 1. XRD Spectra for $Sr_{1-x}La_{2x/3}TiO_3$ ceramics sintered in air. The intensities have been normalised to the (110) main peak of perovskite phase. The peaks from orthorhombic phase are labelled by circles. The first peak in the XRD spectrum for x90 (at 2θ ≈ 11.36°) is due to cation/vacancy ordering along the c-direction. From X10 to X90 the weighted profile R factor values decrease from 15.0 to 7.4; the Goodness of fit values vary from 1.27 to 1.56.
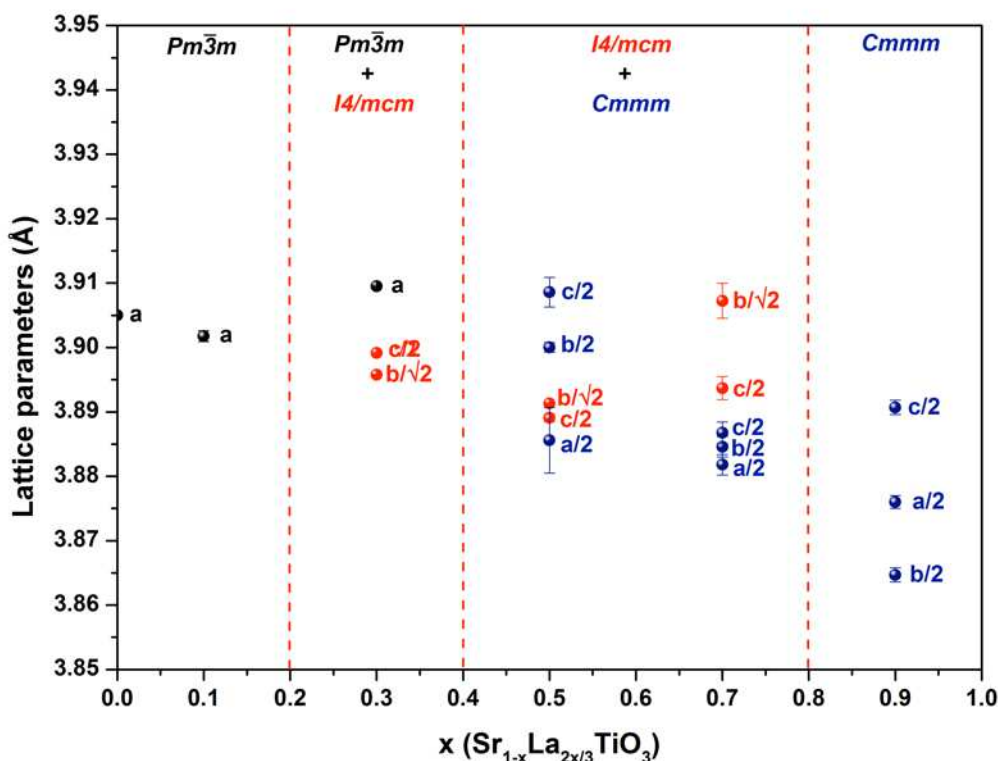
Figure 2. Refined lattice parameters for $Sr_{1-x}La_{2x/3}TiO_3$ ceramics sintered in air as a function of La content.

Electron Microscopy.

Figure 3 shows a typical SEM micrograph of the microstructure of $Sr_{1-x}La_{2x/3}TiO_3$ ceramics; this image is for x10A. For all compositions, the grains are equiaxed in shape with narrow grain size distributions. Most individual grains are in the 5–10 μm range.
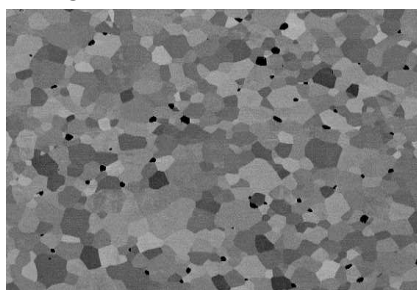

Figure 3 SEM micrograph of air sintered sample x10A

To define the effect of A-site vacancies on the thermal conductivity of $SrTiO_3$, detailed TEM-

SADP (Selected Area Diffraction Pattern) for the major zone axes and atomically resolved STEM-HAADF-EELS characterization of the air sintered ceramic x90A (having the highest vacancy content) were performed. Above 10 mole%, $SrTiO_3$ stabilizes the $La_{2/3}TiO_3$ end member and gives a single phase ceramic, with an orthorhombic *Cmmm* unit cell where lattice parameters (a= 7.74Å, b=7.7204Å and c=7.782Å) are doubled compared to those of the $SrTiO_3$ cubic cell. The cell doubling results from cation/vacancy ordering and out of phase octahedral tilting.[42] SADPs for two main zone axes [001] and [100] for x90 are shown in Figure 4(a,b), and confirm the orthorhombic symmetry with *Cmmm* as space group with a ≈ b ≈ c ≈ 2a_perovskite, where 2a_perovskite is the size of the cubic *Pm3̄m* parent unit cell. Diffraction patterns for samples sintered under reducing conditions are very similar.

The [100] schematic projection of orthorhombic *Cmmm* structure for x90 deduced from XRD analysis is presented in Figure 3c. The core of the structure is the tilted Ti-oxygen octahedra. The 4g

5

A1-sites are fully occupied by La and the 4h A2-sites partially occupied by La (40%); together they are arranged in a layered manner, with the unit cell indicated on Figure 4c.

Inspecting Figure 4c carefully, the configurations to be used for the simulations can be easily understood: configuration xNRand has La, Sr, and vacancies randomly distributed across all A-sites; in configuration xNLaSr the centre layer would contain La, Sr, and vacancies whereas the top and bottom layers would contain only La ions; in configuration xNLaV the centre layer would contain La and vacancies whereas the top and bottom layers would contain La and Sr ions.
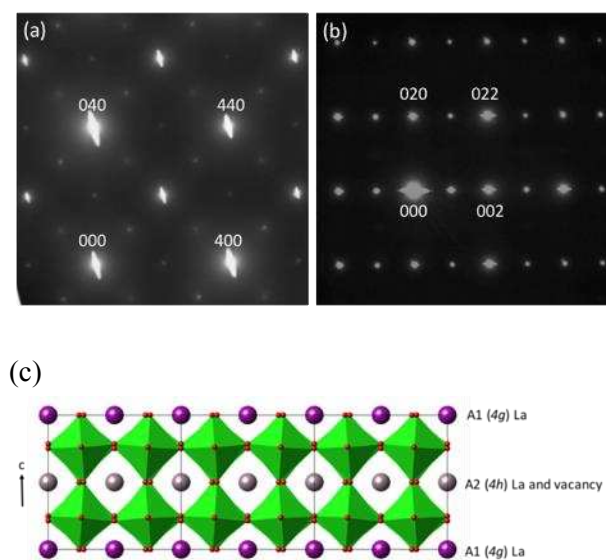
Figure 4. SADPs for ceramic X90A: (a) [001] and (b) [100] zone axes, and (c) schematic representation of the crystal structure of x90A along the a-axis.

As the X-ray data are volume-averaged (the typical minimum value for crystallite size used in the structural refinement is ~ 50nm), atomic resolution characterization was performed to observe atomic scale features. The HAADF–EELS data for ceramic x90 (Figure 5) provides direct evidence of the layered distribution of La cations suggested in the schematic projection (Figure 4c). Figure 5a is a HAADF image, obtained by rigid registration of a series (typically 20) of images of the same area acquired in rapid succession – thus providing higher signal-to-noise and precision. Such images will hereafter be denoted 'stacked images' for simplicity. The image shows alternating rows of atomic columns with differing intensities (i.e. A1, La1 and A2, La2 sites of the structure). However, intensity profiles for the two rows with different intensities (Figure 5a) show small variations for the intensity for A1 rows (Figure 5b) with much larger

differences for the intensity of rows of A2 atomic columns (Figure 5c), suggesting that the distribution of La and vacancies is not uniform. There are therefore atomic columns with high La concentration and atomic columns with high vacancy content (arrowed in Figure 5c). Figure 5 (d,e,f) presents EELS maps for La, obtained by integrating the EELS signal acquired at each point over a suitable energy window above the La-M$_{4,5}$ ionisation edge, after subtraction of the decaying background intensity using a power law model. These maps confirm that the variation of intensity in HAADF images specifically for the A2-sites corresponds to a relative variation in La content of the atomic columns. This variation in the La and vacancy content in A2-sites is known to cause further non-uniform displacement of B-site cations (Ti) and Ti-O octahedral distortions which already exist in A-site deficient perovskites,[43] manifesting itself as non-uniformity and disorder in the structure. This is thought to contribute to additional phonon scattering specifically at low temperatures thus creating temperature-stable, glass-like thermal conductivity behavior. It should be noted that HAADF images for ceramic x90 are reminiscent of HAADF images of LaAlO$_3$ stabilized La$_{2/3}$TiO$_3$, that we reported for the first time, showing the vacancies in a A-site deficient perovskite using HAADF imaging.[26, 31] It also resembles the Z-contrast images of recently published data for CaTiO$_3$ stabilized La$_{2/3}$TiO$_3$.[44] perovskite using HAADF imaging.[26, 31]

Following the confirmation of the crystal structure of ceramic x90, further analysis was performed to investigate the sub-grain features of the material. Figure 6 presents [100] zone axis TEM data for x90. The material is characterized by a high density of twins (Figure 6a). On the basis of (currently unpublished) work on the related (Sr,Pr)TiO$_3$ system we expect the phase transformation induced twin boundaries to be present in all the compositions of this study except for cubic x10. Full analysis to confirm this prediction would require a substantial separate investigation. HRTEM data for x90 for one of the twin boundaries and the corresponding Fourier Transform (FFT) for the two domains and their boundary are shown in Figure 6b. The FFT for both domains can be indexed as corresponding to the [100] zone axis of orthorhombic *Cmmm* (as shown in Figure 3b), which are rotated 90º to each other to form the twin boundary. This symmetry-breaking, phase-transition-induced type of twin boundary has been frequently observed in orthorhombic perovskites[45] and may contribute, by additional phonon scattering, to reducing thermal conductivity. In our recent experimental and computational study of the CaMnO$_3$ based thermoelectric,[12,46] this proposal has been verified. In addition to 90º

rotational twin boundaries, antiphase type domain boundaries were observed in the microstructure of x90; an example is shown in Figure 6c. It is characterized by movement of the two domains with a displacement vector of 1/2 of the length of the c axis. This type of boundary has been observed in the microstructure of orthorhombic perovskites (CaTiO$_3$ based compositions) and attributed to antiparallel A-site cation movement or, out of phase rotation of oxygen octahedra.[45-47] The presence of antiphase boundaries may also have positive effects on the reduction of thermal conductivity by providing additional phonon scattering sites.
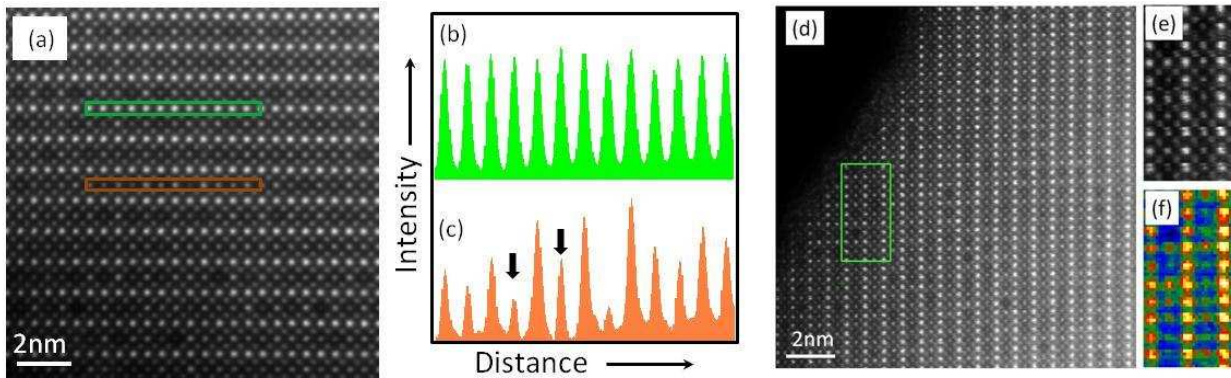
Figure 5. [100] zone axis HAADF-EELS data for x90A sample: (a) stacked HAADF image, and intensity profiles for A1 (b) and A2 site (c); (d), HAADF image, (e) HAADF survey and (f) La EELS M$_{4,5}$ map.
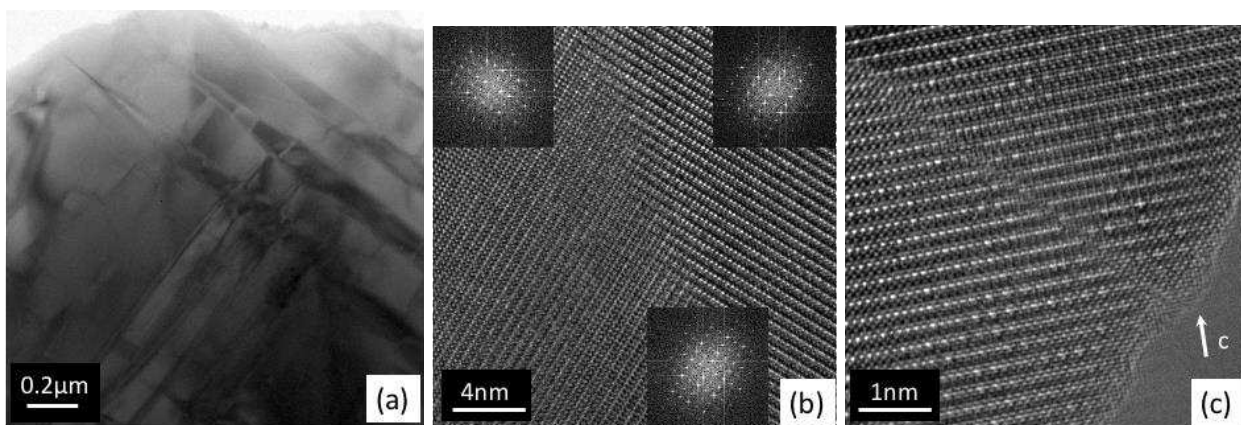
Figure 6. TEM data for sub-grain features in ceramic x90A: (a) TEM image showing twinned microstructure; (b) HRTEM image of a twin boundary; (c) HRTEM image of an antiphase boundary.
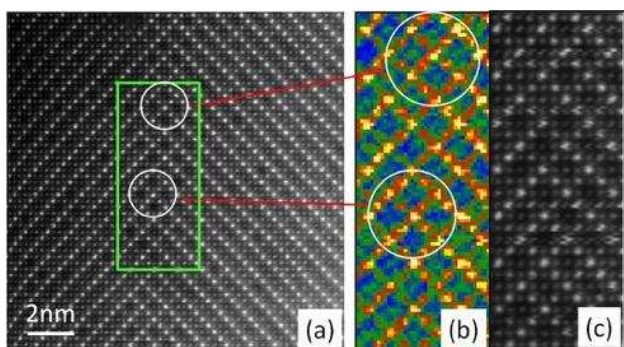
Figure 7. [100] HAADF and EELS data for ceramic x90A containing a rotational twin boundary: (a) HAADF image, (b) La EELS map, (c) HAADF survey.

Figure 7 illustrates [100] HAADF - EELS data for a 90° rotational twin boundary in ceramic x90. HAADF imaging revealed clustering of vacancy rich columns forming a larger unit cell with dimensions of $2a_{orthorhombic}$ x $2a_{orthorhombic}$ = $4a_{perovskite}$ at the twin boundary (Figure 7a, circled). From HRTEM images of grains of composition Sr$_{0.25}$La$_{0.5}$TiO$_3$ in the SrTiO$_3$-La$_{2/3}$TiO$_3$ system (equivalent to x80 in the current notation), Battle et al.[30] reported a similar phenomenon for the clustering of vacancies with dimensions $2a_{perovskite}$ x $a_{perovskite}$. For the present data, the corresponding La EELS map from the grain boundary, including the region with clustering of vacancies, is shown in Figure 7(b,c), verifying the conclusion inferred from the HAADF image (Figure 7a). This localized clustering of vacancies and formation of larger unit-cells will create non-uniformity in the matrix of the material and, as in the arguments highlighted above, will act as additional phonon scattering centers, thus influencing the thermal conductivity of the material.

7

The final part of electron microscopy investigation was focused on the $SrTiO_3$ rich-compositions, x50 and x30, that have shown the best thermoelectric properties (highest ZT values) in the $SrTiO_3$-$La_{2/3}TiO_3$ system. [41, 48] HAADF imaging and chemical mapping (Figure 8) again shows the distributions of both vacancies and La cations for x50 and x30. Evidence of vacancy clustering was observed for composition x50. Examples of vacancy clustering are shown within the ellipsoids in Figure 8(a). No evidence for vacancy clustering was observed for x30.
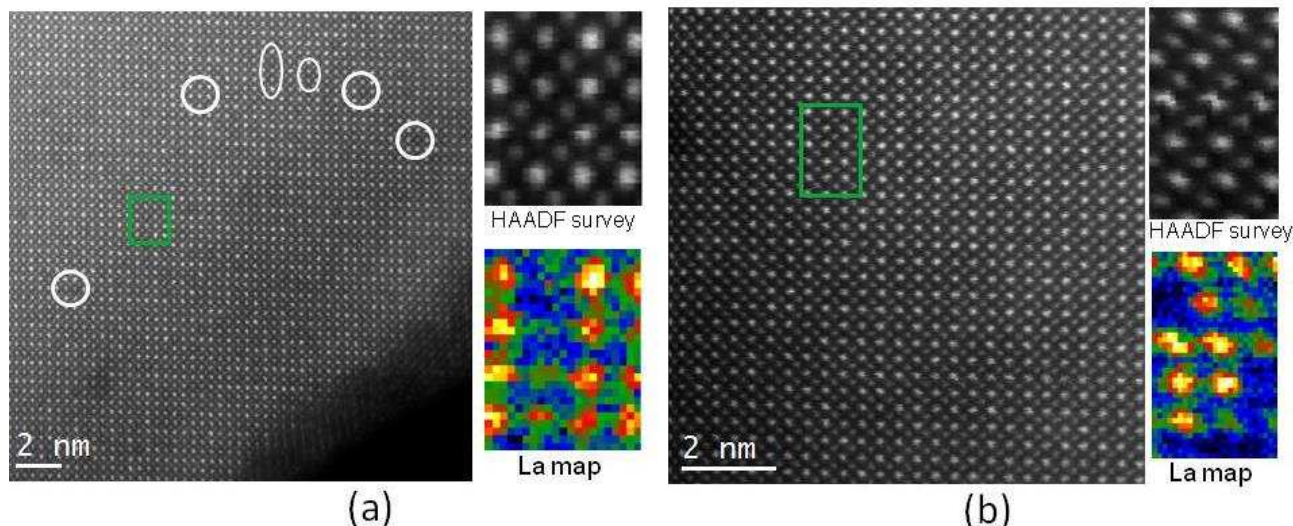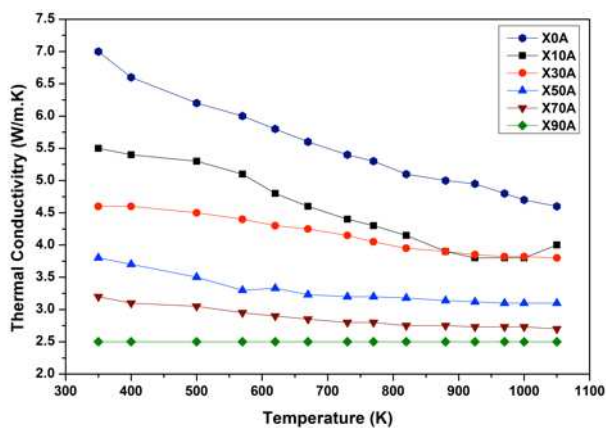

Figure 8. [100] HAADF - EELS data for ceramics: (a) x50 and (b) x30. Examples of vacancy rich columns are shown inside circles in the HAADF image for x50 (a).

Thermoelectric Properties of Experimentally Synthesized Samples:

A; Samples Sintered in Air Atmosphere.

The thermal conductivity for all the ceramics as a function of temperature is presented in Figure 9.

Figure 9. Thermal conductivity of $Sr_{1-x}La_{2x/3}TiO_3$ (X0A to X90A) as a function of temperature

The measurements demonstrate that altering the composition of this A-site deficient perovskite has the effect of reducing thermal conductivity of $SrTiO_3$ (Figure 9). Above 30 mole% substitution of $La_{2/3}TiO_3$ into $SrTiO_3$ (i.e. x30 and higher), the materials exhibit near glass-like thermal conductivity, with end member, x90 showing fully temperature stable behavior with a low thermal conductivity of 2.5 W/K.m. At lower levels of substitution this temperature-invariant behavior disappears; however the thermal conductivity is still lower than that of undoped $SrTiO_3$, mainly due to the substitution of Sr by the heavier La ions and the presence of significant numbers of vacancies. The marked decrease of thermal conductivity from sample x30 to x50 can be explained by the higher content of orthorhombic phase which in turn introduces more phonon scattering points. There is also evidence of increased vacancy clustering when moving from x30 to x50, demonstrated in the electron microscopy results.

This low and glass-like thermal conductivity arises from the following structural characteristics: (i) the presence of heavy La cation and vacancies in the structure; (ii) presence of a layered structure which enhances phonon scattering; (iii) a non-uniform distribution of La and vacancies in the intermediate layer of the structure leading to non-uniform Ti-O octahedral distortion and Ti-O bond lengths, creating a non-uniform distribution of atomic scale features in the matrix of the material; and (iv) the presence of twin and antiphase boundaries. The first three factors dominate, with the presence of twin and antiphase boundaries playing a relatively minor role because of the large twin boundary spacing (in excess of 20 nm). [49]

By cooling the samples slowly after sintering the contribution from Ti^{3+} was minimized. Across all compositions the estimated contribution from electronic conductivity is less than 0.03% of total thermal conductivity. The thermal conductivity data reported by Popuri et al.[18] for x20 and x40 are consistent with our data presented in Figure 9. Furthermore, the data of Popuri et al.[18] shows glass-like thermal conductivity for a sample composition of x = 0.8 exhibiting some degree of vacancy disorder.
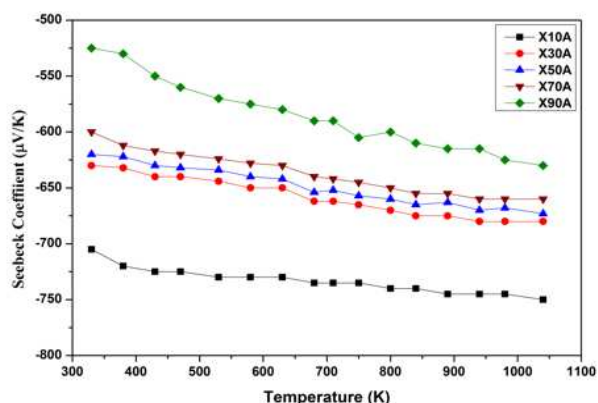

Figure 10. Seebeck coefficients of the air sintered samples.

All the ceramics exhibit a negative Seebeck coefficient indicating n-type conduction (Figure 10). The data show a steady increase in magnitude with temperature; this is typical for $SrTiO_3$ ceramics and reflects the decrease in chemical potential with temperature.[50] The magnitude of the Seebeck coefficient decreases with increased La content. There is a large decrease from composition x30A to x90A as the perovskite structure changes from cubic to tetragonal to orthorhombic. However, the A-site deficient perovskite, composition x90A, still shows high Seebeck values in the range of -520 to -650 µV/K. The changes in the Seebeck coefficients are related to the density of states (DOS) about the Fermi level; a high order of symmetry in a crystal will give a steep DOS. The structural phase changes will break the crystal symmetry and therefore lead to reductions in Seebeck coefficients at such transitions.

As expected, all the air sintered ceramics show very low electrical conductivity in the range 0.2 to 0.8 S/cm at temperatures of 325 to 1030K. To evaluate the effect of electrical conductivity, thermal conductivity and Seebeck coefficient on the thermoelectric figure of merit, ceramic samples of the same compositions were prepared in a reducing atmosphere.

B; Thermoelectric Properties of Samples Sintered in Reducing Atmosphere.

The temperature dependence of the electrical conductivity of the reduced ceramics is shown in Figure 11. The three orders of magnitude increase in the electrical conductivity of the reduced samples compared to that of the air sintered samples is due to a reduction of Ti^{4+} to Ti^{3+}. The additional electrons in the lattice increase the carrier concentrations and therefore the electrical conductivity. This data shows typical electrical conductivity behavior of semiconducting ceramics. There is an initial increase in the conductivity due to thermal excitation of the electrons followed by a decline in conductivity due to electron phonon scattering. The x30H samples exhibit the highest electrical conductivity. Additional levels of La doping lead to significant reductions in electrical conductivity.
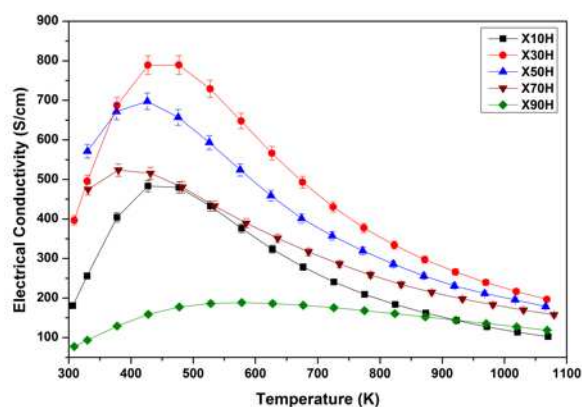
Figure 11. Temperature dependence of Electrical conductivity of the reduced samples.

The thermal conductivity of the reduced ceramics as a function of temperature is presented in Figure 12. The trend is similar to that observed for the air sintered samples, although thermal conductivities of the reduced samples are very slightly higher; this is related to the higher carrier concentrations, which give rise to higher electrical conductivities (Figure 11). Thermal conductivity data for heavily doped compositions (x50 to x90) are almost temperature invariant, with X90 exhibiting the lowest thermal conductivity values (Figure 12) as was the case for the air-sintered samples (Figure 9).

9
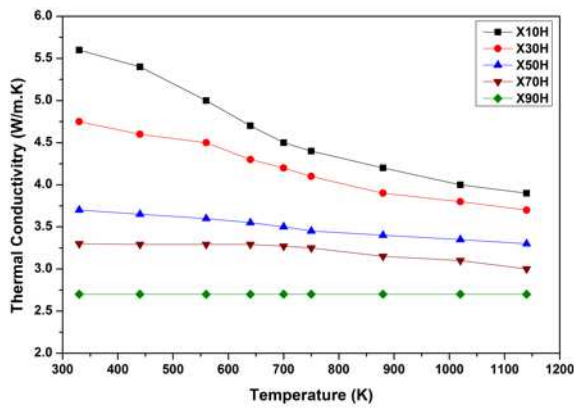
Figure 12. Thermal conductivity for reduced samples.

The Seebeck coefficients for the reduced samples (Figure 13) display the same basic trends as the air sintered samples (Figure 10) but, as expected, the magnitude is substantially reduced for the reduced samples. Again, the reduction in Seebeck coefficient is caused by the increase in carrier concentration, which in turn is caused by the reduction of Ti^{4+} to Ti^{3+}. The Seebeck coefficients for individual samples increase with increasing La/vacancy content, x90H being the lowest and x10H being the highest. The net changes in electrical conductivity and Seebeck coefficient combine to give the temperature dependence in the important thermoelectric parameter, the power factor (Figure 14). For most compositions, there is a peak in the power factor between 500 K and 600 K due to the electrical conductivity peak at these temperatures (Figure 12). Whilst sample x10H exhibits the highest power factor of this series of composition, 0.0016 W/m.K^2 at 475 K, followed by a rapid decline at higher temperatures, both x30H and x50H retain high power factors over a wider range of temperatures.
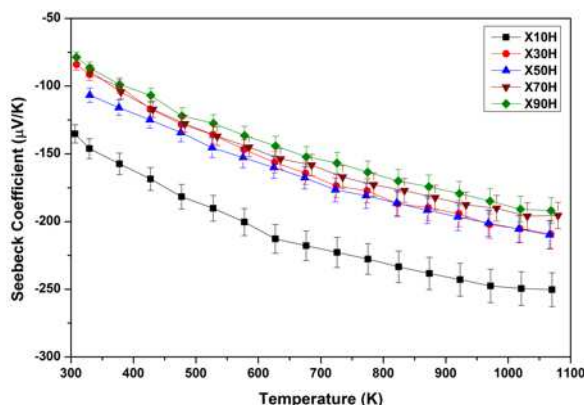

Figure 13. Temperature dependence of Seebeck coefficient for reduced samples.
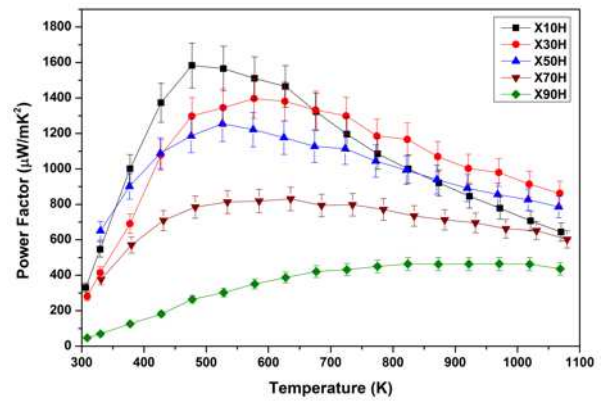
Figure 14. Temperature dependence of the power factor for reduced samples.

Finally, the thermoelectric figure of merit of all reduced ceramics show a steady increase with increasing temperature (Figure 15). The ceramics x10H, x30H and x70H all show a similar trend in ZT from room temperature to 500 K where the electrical conductivity peaks (Figure 12). Above 500 K, the ZT increases with temperature for compositions x30H, x50H and X70H but it decreases for the composition with the lowest La/vacancy content (i.e. x10H). The decrease in thermal conductivity with respect to composition dominates the trend in the overall thermoelectric figure of merit. The maximum dimensionless figure of merit achieved is 0.27 at 870 K for x50H. The data show that for $SrTiO_3$ improving the figure of merit is achieved mainly by reducing thermal conductivity through introducing La and A-site vacancies into the lattice.
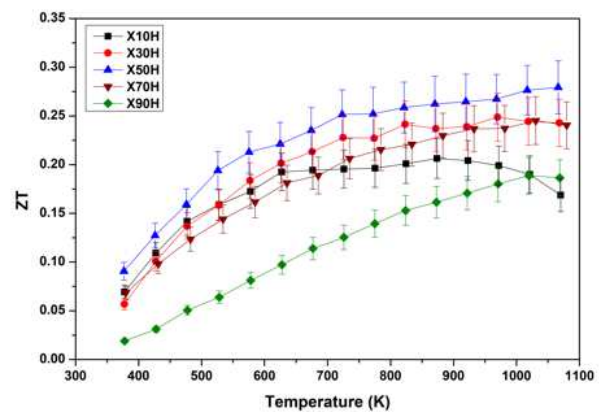
Figure 15. Dimensionless Figure of Merit for reduced samples.

Thermal Properties of Model Structures using Molecular Dynamics.

Computational techniques are used here to complement the thorough experimental characterization presented above, with the goal of determining which factors control the complex

10

behavior of a specific property. Thus, we have calculated the thermal conductivity of model systems at three compositions x20, x50, and x90. For each composition, we have made up three structures: a random (labelled 'Rand') distribution of Sr, La and A-site vacancies across all A-sites; a layered system whereby one layer is fully occupied by La and the other layer is filled with the remaining La, Sr, and A-site vacancies (labelled 'LaSr'); a layered system whereby one layer is fully occupied by La and Sr and the other layer is filled with the remaining La and A-site vacancies (labelled 'LaV'). This gives us the opportunity to determine unambiguously whether the formation of layers in the perovskite structure or/and the doping is the cause of reduction in thermal conductivity as a function of La and A-site vacancies contents.

The calculated thermal conductivity values from 500 K to 1100 K of all model structures are presented in Figure 16. The compositions x20, x50, and x90 all exhibit a decrease in the thermal conductivity as a function of temperature for all types of structures. This is expected for the thermal conductivity as phonon-phonon scattering with increased temperature leads to a decrease in thermal conductivity. All x20 models show the largest thermal conductivity whilst all x90 models have the smallest thermal conductivity across the entire temperature range. The differences between these models, regardless of structure type, depend on the La:Sr:A-site vacancy ratios. As the La and A-site vacancy concentrations increase, the thermal conductivity decreases. Although Kovalevsky et al.[41] and Yu et al.[48] proposed that oxygen vacancies may have an impact on the thermal conductivity, our calculations cannot directly support this. Our model structures intentionally do not include or take into account the presence of oxygen vacancies and therefore do not provide any further insight into the formation of oxygen vacancies as a mechanism for reduction of the thermal conductivity. The computational models were made to resemble the experimental samples synthesized in air (such as sample x30A and x70A etc. in Figure 9), and we therefore assumed that there were no oxygen vacancies. In our models the only variable is therefore the La(2x/3):Sr(1-x) ratio, and thus, we infer that the reduction in the thermal conductivity intrinsically arises from the introduction of La and A-site vacancies, and not the stabilization of oxygen vacancies. Although the latter may be a feasible mechanism when the material is synthesized in reducing conditions, the primary focus of this work is to investigate the effect of A-site vacancies alone.

Figure 16 also allows the evaluation of the effect of structural type on thermal conductivity when the composition is constant. At the lowest La content (x20 - Figure 16 a,b,c) the thermal conductivity does not show any differences between the different models, whether the distribution of cations and A-site vacancies is random or layered. This lack of variation is most certainly due to the low concentration of dopants. Given that 80 % of the A-sites are filled with Sr, the three models can arguably be equally considered randomly or layered distributed structures. Therefore, the phonons that can propagate are unchanged by the ordering of the remaining 20 % of species on the A-sites. However, the x20 composition shows that a greater amount of doping is necessary to lower the thermal conductivity although it does not tell us whether it is the formation of layers in the perovskite structure that causes the change in thermal conductivity.

At the mid-range composition of x50, the thermal conductivity (Figure 16a,b,c) shows some variation, especially for the x50LaSr model (2.9 W/m.K at 500 K), which displays a small increase in the thermal conductivity over the entire temperature range compared to x50LaV (2.7 W/m.K at 500 K) and x50Rand (2.7 W/m.K at 500 K). Given this small variation in the results, it is not possible to draw any strong conclusions.

At the highest La content, x90 (Figure 16 a,b,c), the thermal conductivities of the different model structures show clear differences. There is a clear increase in the thermal conductivity for x90LaSr (2.5 W/m.K at 500 K) across the entire temperature range, whereas x90LaV (2.3 W/m.K at 500 K) and x90Rand (2.1 W/m.K at 500 K) have lower thermal conductivity. The layered structure x90LaSr contains alternating layers of A-sites fully filled with La, such that every other layer contains the remaining cations and A-site vacancies. Rather differently, the layered structure x90LaV contains layers of A-sites filled with La and all the A-site vacancies, with every other layer containing the remaining cations. This indicates that the formation of the layered structure due to the increased doping content and the distribution of vacancies within the layers are the causes behind the change in thermal conductivity. In contrast to x90LaV where a single type of defect exists within each layer, in x90LaSr there are completely filled A-sites layers. The latter will therefore have reduced phonon scattering within the layer compared to the former due to the lack of A-site vacancies, and thus this causes the overall thermal conductivity to increase. Indeed inspection of the modeling data in Fig. 16 suggests that the main impact comes from the concentration of the A-site vacancies, while the differences between the different La and A-site vacancy distribution models are much smaller.

11

Interestingly, our results indicate that the model x90Rand has the lowest thermal conductivity. Whilst x90LaV contains a single type of defect within each layer, the x90Rand has La, Sr, and vacancies randomly distributed across all A-sites in every layer.

Comparison with Experimental Data. Since our primary goal is to investigate the effect of A-site vacancies on the thermal conductivity, we have used the computational data to interpret the experiments (Figure 9). As several structures are used for our computational investigation, the first step is to determine the most suitable structure to compare with the corresponding experimental results. Obviously for the x20 calculations, any of the computational model structures, which can be considered equivalent, are viable as there are no marked differences in the resulting thermal conductivity; therefore the x20Rand results are selected as these represent the most similar structure to what is observed experimentally. The experimental samples that can be closely compared with the computational x20 data are either x10 or x30, which fall on either side of this composition. As x10 exhibits different behavior to the rest of the ceramics in the series (i.e. a steeper gradient in the range 500 K to 1100 K due to the small number of defects), we use x30 ceramics for comparison. For the experimental x50, we use x50LaSr as a comparison, as this structure contains A-site vacancies / La clusters as seen experimentally (Figure 8a). Finally, for the ceramic x90, the calculated results x90LaSr are selected for comparison as, experimentally, only a layered structure can be synthesized. Indeed, the layered structure in the experimental ceramic consists of a fully occupied La layer with the remaining cations partially filling every other layer, which is best represented by the computational x90LaSr structure. So, to summarize we will use x20Rand, x50LaSr and x90LaSr to compare to experimental data for ceramics x20, x50 and x90 respectively.

The comparison (Figure 17) between the computational (filled symbols) and the experimental (hollow symbols) thermal conductivity data of samples synthesized in air (Figure 9) from 500 K to 1100 K shows the same qualitative trends. The thermal conductivity for both datasets decreases as the temperature increases due to phonon-phonon scattering becoming the dominant mechanism over phonon-defect scattering.

The magnitude of the experimental data is different from the simulated data. This is expected as we are using very simple computational models that do not contain the complexity of the experimental samples. From a computational point of view, this was necessary if we were to disentangle the effect of doping and the formation of layered perovskite materials. Furthermore we use classical molecular dynamics calculations which use a potential model (a set of parameterized analytical equations) which reproduce the properties of materials although shifted in magnitude. This is common for this kind of calculations, but it is also common for calculations using high level of theory such as ab initio calculations.
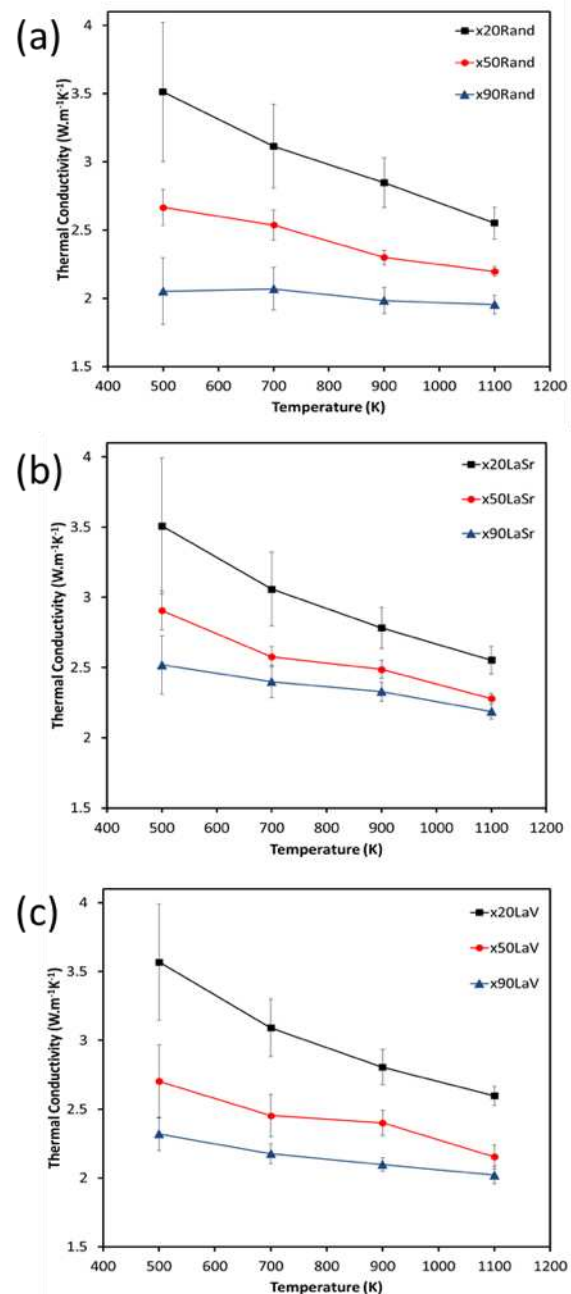
Figure 16 The thermal conductivity values of the x20, x50 and x90 models in the temperature range of 500-1100K. (a) A random (labelled 'Rand') distribution of Sr, La and vacancies across all A-sites. (b) A layered system whereby one layer is fully occupied by lanthanum and the other layer is filled with the remaining lanthanum, strontium, and vacancies (labelled 'LaSr'). (c) A layered

system whereby one layer is fully occupied by lanthanum and strontium and the other layer is filled with the remaining lanthanum, and vacancies (labelled 'LaV').

The thermal conductivity for both the experimental and computational data decreases with increasing La and A-site vacancy contents due to increased phonon scattering from the vacant sites as well as the larger ion size of the La cations. The decrease in thermal conductivity amongst the computational structures is also in line with the one displayed by the experimental ceramics. This is consistent with the increase in doping concentration and corresponding phonon scattering between x30 and x50 but also a component due to the formation of layers in the perovskite structure between x50 and x90. Since thermal conductivity is one of the main factors controlling thermoelectric performance we now have significant insight into routes to designing and synthesizing improved perovskite-structured thermoelectrics.
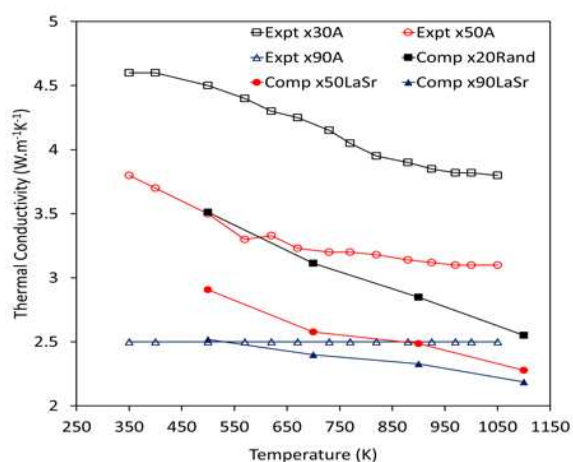
Figure 17. The thermal conductivities of the computational results (filled symbols) with the corresponding experimental results (hollow symbols). The computational results were chosen to best match the crystal structure of the experimental ceramics.

CONCLUSIONS

We have employed experimental and computational techniques, including atomic-resolution STEM-HAADF and STEM-EELS, and molecular dynamics modelling to disentangle the role of La doping in inducing A-site vacancies and of the formation of layers when increasing La content, in $Sr_{1-x}La_{2x/3}TiO_3$ ceramics ($0.0 \leq x \leq 0.9$).

At low La content ($x < 0.3$) the ceramics have a cubic structure (space group $Pm\bar{3}m$) and A-site vacancies randomly distributed. At intermediate La content, there is a move to vacancy clustering ($x \sim 0.5$) and the ceramics are characterized by a mixture of crystal structures (cubic, tetragonal and orthorhombic). Finally, for high La content ($x = 0.9$) there is a transition to orthorhombic symmetry, with doubling of axes along all three lattice directions (with $a^-b^0c^0$ tilt system and space group *Cmmm*), ordering of vacancies and La, and segregation of vacancies at 90º twin boundaries leading to the formation of localized supercells.

The thermal conductivity for both the experimental and computational data decreases with increasing La and A-site vacancy contents due to increased phonon scattering from the vacant sites as well as the larger ion size of La. The clear jump between x30 and x50 could be related to the structural transition from cubic + tetragonal (X30) to orthorhombic (X50). High La doped ($x = 0.9$) samples exhibit the lowest thermal conductivity. The reduction is enhanced by localized clustering of vacancies and the formation of larger unit-cells, thereby creating further non-uniformity in the matrix of the material that act as additional phonon scattering centers.

We infer that the reduction in the thermal conductivity intrinsically arises from the introduction of La and A-site vacancies, and the formation of the layered structures and not the stabilization of oxygen vacancies (all our samples are synthesized in air). However, our modelling indicates that the thermal conductivity at high La content can be further lowered when La and vacancies are distributed randomly rather than ordered in layered structures. This suggests that doping is a more efficient way to lower the thermal conductivity compared to the formation of layers. Hence, we suggest that synthetic work is needed to further advance the nanostructuring of La doped $SrTiO_3$.

AUTHOR INFORMATION

Corresponding Authors

*Email: Robert.Freer@manchester.ac.uk
*Email: S.C.Parker@bath.ac.uk

HPC Orion at the University of Huddersfield. SuperSTEM is the EPSRC National Facility for Advanced Electron Microscopy, supported by EPSRC. All data supporting this study are openly available from the University of Manchester data archived at DOI xxxx.

REFERENCES

(1) Snyder, G. J.; Toberer, E. S. Complex Thermoelectric Materials. *Nat. Mater.* **2008,** 7, 105-114.

(2) Koumoto, K.; Wang, Y. F.; Zhang, R. Z.; Kosuga, A.; Funahashi, R. Oxide Thermoelectric Materials: A Nanostructuring Approach. *Annu. Rev. Mater. Res.* **2010,** 40, 363-394.

(3) Fergus, J. W. Oxide Materials for High Temperature Thermoelectric Energy Conversion. *J. Eur. Ceram. Soc.* **2012,** 32, 525-540.

(4) Norman, C.; Azough, F.; Freer, R. In *Thermoelectric Materials and Devices*; The Royal Society of Chemistry: 2017; 60-82.

(5) Funahashi, S.; Nakamura, T.; Kageyama, K.; Ieki, H. Monolithic Oxide–Metal Composite Thermoelectric Generators for Energy Harvesting. *J. Appl. Phys.* **2011,** 109, 124509.

(6) Terasaki, I.; Sasago, Y.; Uchinokura, K. Large Thermoelectric Power in $NaCo_2O_4$ Single Crystals. *Phys. Rev. B* **1997,** 56, 12685-12687.

(7) Baran, J. D.; Molinari, M.; Kulwongwit, N.; Azough, F.; Freer, R.; Kepaptsoglou, D.; Ramasse, Q. M.; Parker, S. C. Tuning Thermoelectric Properties of Misfit Layered Cobaltites by Chemically Induced Strain. *J. Phys. Chem. C* **2015,** 119, 21818-21827.

(8) Baran, J. D.; Kepaptsoglou, D.; Molinari, M.; Kulwongwit, N.; Azough, F.; Freer, R.; Ramasse, Q. M.; Parker, S. C. Role of Structure and Defect Chemistry in High-Performance Thermoelectric Bismuth Strontium Cobalt Oxides. *Chem. Mater.* **2016,** 28, 7470-7478.

(9) Combe, E.; Funahashi, R.; Barbier, T.; Azough, F.; Freer, R. Decreased Thermal Conductivity in $Bi_2Sr_2Co_2O_x$ Bulk Materials Prepared by Partial Melting. *J. Mater. Res.* **2016,** 31, 1296-1305.

(10) Bocher, L.; Aguirre, M. H.; Robert, R.; Logvinovich, D.; Bakardjieva, S.; Hejtmanek, J.; Weidenkaff, A. High-Temperature Stability, Structure and Thermoelectric Properties of $CaMn_{1-x}Nb_xO^3$ Phases. *Acta Mater.* **2009,** 57, 5667-5680.

(11) Molinari, M.; Tompsett, D. A.; Parker, S. C.; Azough, F.; Freer, R. Structural, Electronic and Thermoelectric Behaviour of $CaMnO_3$ and $CaMnO_{3-\delta}$. *J. Mater. Chem. A* **2014,** 2, 14109-14117.

(12) Srivastava, D.; Azough, F.; Freer, R.; Combe, E.; Funahashi, R.; Kepaptsoglou, D. M.; Ramasse, Q. M.; Molinari, M.; Yeandel, S. R.; Baran, J. D.; Parker, S. C. Crystal Structure and Thermoelectric Properties of Sr-Mo Substituted $CaMnO_3$: A Combined Experimental and Computational Study. *J. Mater. Chem. C* **2015,** 3, 12245-12259.

(13) Ohta, H.; Sugiura, K.; Koumoto, K. Recent Progress in Oxide Thermoelectric Materials: P-Type $Ca_3Co_4O_9$ and N-Type $SrTiO_3$. *Inorg. Chem.* **2008,** 47, 8429-8436.

(14) Muta, H.; Kurosaki, K.; Yamanaka, S. Thermoelectric Properties of Reduced and La-Doped Single-Crystalline SrTiO3. *J Alloy Compd* **2005,** 392, 306-309.

(15) Okuda, T.; Nakanishi, K.; Miyasaka, S.; Tokura, Y. Large Thermoelectric Response of Metallic Perovskites: $Sr_{1-x}La_xTiO_3$ (0<~x<~0.1). *Phys. Rev. B* **2001,** 63, 113104.

(16) Ohta, S.; Nomura, T.; Ohta, H.; Koumoto, K. High-Temperature Carrier Transport and Thermoelectric Properties of Heavily La-or Nb-Doped $SrTiO_3$ Single Crystals. *J. Appl. Phys.* **2005,** 97, 034106.

(17) Jackson, S. S.; Azough, F.; Freer, R. Neodymium-Strontium Titanate: A New Ceramic for an Old Problem. *J. Electron. Mater.* **2014,** 43, 2331-2336.

(18) Popuri, S. R.; Scott, A. J. M.; Downie, R. A.; Hall, M. A.; Suard, E.; Decourt, R.; Pollet, M.; Bos, J. W. G. Glass-Like Thermal Conductivity in $SrTiO_3$ Thermoelectrics Induced by a-Site Vacancies. *RSC Adv.* **2014,** 4, 33720-33723.

(19) Mehdizadeh Dehkordi, A.; Bhattacharya, S.; Darroudi, T.; Graff, J. W.; Schwingenschlögl, U.; Alshareef, H. N.; Tritt, T. M. Large Thermoelectric Power Factor in Pr-Doped $SrTiO_{3-\delta}$ Ceramics Via Grain-Boundary-Induced Mobility Enhancement. *Chem. Mater.* **2014,** 26, 2478-2485.

(20) Yeandel, S. R.; Molinari, M.; Parker, S. C. Nanostructuring Perovskite Oxides: The Impact of $SrTiO_3$ Nanocube 3D Self-Assembly on Thermal Conductivity. *RSC Adv.* **2016,** 6, 114069-114077.

(21) Azough, F.; Cernik, R. J.; Schaffer, B.; Kepaptsoglou, D.; Ramasse, Q. M.; Bigatti, M.; Ali, A.; MacLaren, I.; Barthel, J.; Molinari, M.; Baran, J. D.; Parker, S. C.; Freer, R. Tungsten Bronze Barium Neodymium Titanate ($Ba_{6-3n}Nd_{8+2n}Ti_{18}O_{54}$): An Intrinsic Nanostructured Material and Its Defect Distribution. *Inorg. Chem.* **2016,** 55, 3338-3350.

(22) Azough, F.; Freer, R.; Yeandel, S. R.; Baran, J. D.; Molinari, M.; Parker, S. C.; Guilmeau, E.; Kepaptsoglou, D.; Ramasse, Q.; Knox, A.; Gregory, D.; Paul, D.; Paul, M.; Montecucco, A.; Siviter, J.; Mullen, P.; Li, W.; Han, G.; Man, E. A.; Baig, H.; Mallick, T.; Sellami, N.; Min, G.; Sweet, T. $Ba_{6-3x}Nd_{8+2x}Ti_{18}O_{54}$ Tungsten Bronze: A New High-Temperature N-Type Oxide Thermoelectric. *J. Electron. Mater.* **2016,** 45, 1894-1899.

(23) Srivastava, D.; Azough, F.; Molinari, M.; Parker, S. C.; Freer, R. High-Temperature Thermoelectric Properties of (1−x) $SrTiO_3$ − (x) $La_{1/3}NbO_3$ Ceramic Solid Solution. *J. Electron. Mater.* **2015,** 44, 1803-1808.

(24) Evarestov, R. A.; Blokhin, E.; Gryaznov, D.; Kotomin, E. A.; Maier, J. Phonon Calculations in Cubic and Tetragonal Phases of SrTiO3: A Comparative LCAO and Plane-Wave Study. *Phys. Rev. B* **2011,** 83, 134108.

(25) Azough, F.; Wang, W.; Freer, R. The Crystal Structure of $LaAlO_3$-Stabilized $La_{2/3}TiO_3$ Ceramics: An HRTEM Investigation. *J. Am. Ceram. Soc.* **2009,** 92, 2093-2098.

(26) Zhang, Z.; Lumpkin, G. R.; Howard, C. J.; Knight, K. S.; Whittle, K. R.; Osaka, K. Structures and Phase Diagram for the System $CaTiO_3$–$La_{2/3}TiO_3$. *J. Solid State Chem.* **2007,** 180, 1083-1092.

(27) Howard, C. J.; Lumpkin, G. R.; Smith, R. I.; Zhang, Z. Crystal Structures and Phase Transition in the System $SrTiO_3$– $La_{2/3}TiO_3$. *J. Solid State Chem.* **2004,** 177, 2726-2732.

(28) Howard, C. J.; Zhang, Z. Structures and Phase Transition in the Layered Perovskite $La_{0.6}Sr_{0.1}TiO_3$: A New Orthorhombic Structure Solved from High-Resolution Diffraction in Combination with Group Theoretical Analysis. *J. Phys. Condens. Matter* **2003,** 15, 4543-4553.

(29) Howard, C. J.; Zhang, Z.; Carpenter, M. A.; Knight, K. S. Suppression of Strain Coupling in Perovskite $La_{0.6}Sr_{0.1}TiO_3$ by Cation Disorder. *Phys. Rev. B* **2007,** 76, 054108.

(30) Battle, P. D.; Bennett, J. E.; Sloan, J.; Tilley, R. J. D.; Vente, J. F. A-Site Cation-Vacancy Ordering in $Sr_{1-3x/2}La_xTiO_3$: A Study by HRTEM. *J. Solid State Chem.* **2000,** 149, 360-369.

(31) Azough, F.; Freer, R.; Schaffer, B. Direct Observation of a-Site Vacancies and a Twin Boundary Structure in $La_{2/3}TiO_3$-Based Ceramics Using HAADF/STEM. *J. Am. Ceram. Soc.* **2010,** 93, 1237-1240.

(32) *Topas 4.2 Software*, Bruker AXS: Karlsruhe, Germany.

(33) Green, M. S. Markoff Random Processes and the Statistical Mechanics of Time-Dependent Phenomena. Ii. Irreversible Processes in Fluids. *J. Chem. Phys.* **1954,** 22, 398-413.

(34) Kubo, R. Statistical-Mechanical Theory of Irreversible Processes. I. General Theory and Simple Applications to Magnetic and Conduction Problems. *J. Phys. Soc. Jpn.* **1957,** 12, 570-586.

(35) Plimpton, S. Fast Parallel Algorithms for Short-Range Molecular Dynamics. *J Comput. Phys.* **1995,** 117, 1-19.

(36) Canepa, P. New Insights on Iron and Lead-Based Materials Beyond Density Functional Theory. PhD Thesis, University of Kent, Canterbury, 2012.

(37) McGaughey, A. J. H.; Kaviany, M. J., Molecular Dynamics Calculations of the Thermal Conductivity of Silica Based Crystals. In *8th AIAA/ASME Joint Thermophysics and Heat Transfer Conference, AIAA-2002-3343*, St. Louis, Missouri, 2002.

(38) Watson, G. W.; Kelsey, E. T.; deLeeuw, N. H.; Harris, D. J.; Parker, S. C. Atomistic Simulation of Dislocations, Surfaces and Interfaces in Mgo. *J. Chem. Soc., Faraday Trans.* **1996,** 92, 433-438.

(39) Ali, R.; Izumi, F.; Yashima, M. Neutron Powder Diffraction Study of a Phase Transition in $La_{0.68}(Ti_{0.95}Al_{0.05})O_3$. *J. Am. Ceram. Soc.* **2006,** 89, 3805-3811.

(40) Lu, Z.; Zhang, H.R.; Lei,W.; Sinclair, D.C.; Reaney, I.M. High-Figure-of-Merit Thermoelectric La-Doped A-Site-Deficient $SrTiO_3$ Ceramics, *Chem. Mater.* **2016**, 28, 925-935.

(41) Kovalevsky, A. V.; Yaremchenko, A. A.; Populoh, S.; Weidenkaff, A.; Frade, J. R. Effect of A-Site Cation Deficiency on the Thermoelectric Performance of Donor-Substituted Strontium Titanate. *J. Phys. Chem. C* **2014**, 118, 4596-4606.

(42) Howard, C. J.; Kennedy, B. J.; Woodward, P. M. Ordered Double Perovskites - a Group-Theoretical Analysis. *Acta Crystallogr. Sect. B* **2003,** 59, 463-471.

(43) Jones, G. O.; Thomas, P. A. Investigation of the Structure and Phase Transitions in the Novel a-Site Substituted Distorted Perovskite Compound $Na_{0.5}Bi_{0.5}TiO_3$. *Acta Crystallogr. Sect. B* **2002,** 58, 168-178.

(44) Danaie, M.; Kepaptsoglou, D.; Ramasse, Q. M.; Ophus, C.; Whittle, K. R.; Lawson, S. M.; Pedrazzini, S.; Young, N. P.; Bagot, P. A. J.; Edmondson, P. D. Characterization of Ordering in a-Site Deficient Perovskite $Ca_{1-x}La_{2x/3}TiO_3$ Using STEM/EELS. *Inorg. Chem.* **2016,** 55, 9937-9948.

(45) Wang, Y.; Liebermann, R. C. Electron Microscopy Study of Domain Structure Due to Phase Transitions in Natural Perovskite. *Phys. Chem. Miner.* **1993,** 20, 147-158.

(46) Lowndes, R. Structural and Microwave Dielectric Properties of Ceramics of $Ca_{(1-x)}Nd_{2x/3}TiO_s$. PhD Thesis, The University of Manchester, Manchester, 2012.

(47) Wondratschek, H.; Jeitschko, W. Twin Domains and Antiphase Domains. *Acta Crystallogr. Sect. A* **1976,** 32, 664-666.

(48) Yu, C.; Scullin, M. L.; Huijben, M.; Ramesh, R.; Majumdar, A. Thermal Conductivity Reduction in Oxygen-Deficient Strontium Titanates. *Appl Phys Lett* **2008,** 92, 191911-191911.

(49) Mao, J; Wang, Y.; Liu, Z.; Ge, B.; Ren, Z.; Phonon scattering by nanoscale twin boundaries, Nano Energy, 2017, 32, 174–179

(50) Ohta, S.; Nomura,T.; Ohta, H.; Koumoto, K. High-temperature Carrier Transport and Thermoelectric Properties of Heavily La- or Nb-doped $SrTiO_3$ single crystal, *J Appl Phys* **2005**, 97, 034106.

Table of Contents Graphic